Solar Energy Materials & Solar Cells 289 (2025) 113695

Contents lists available at ScienceDirect

Solar Energy Materials and Solar Cells

journal homepage: www.elsevier.com/locate/solmat

Hidden traces: Insights into how solar cell handling drives damp-heat failures in HJT and TOPCon modules

Chandany Sen *, Haoran Wang, Muhammad Umair Khan, Jiaxin Yang, Ziruo Zhu, Anjie Li, Bram Hoex **

School of Photovoltaic and Renewable Energy Engineering, University of New South Wales, Sydney, NSW, 2052, Australia

ARTICLE INFO

Keywords:
PERC
TOPCon
HJT
Modules
Damp heat
Reliability
Contaminants

ABSTRACT

Tunnel oxide passivated contact (TOPCon) is now the dominant photovoltaic technology and heterojunction (HJT) solar cells are expected to rapidly gain market share due to their superior efficiencies. However, both TOPCon and HJT cells remain vulnerable to humidity-induced degradation, especially when encapsulated in front-glass/rear-backsheet configurations. This study investigates the role of "hidden contaminants" in damp heat (DH)-induced degradation in HJT and TOPCon glass-backsheet modules while observing no such effects in passivated emitter and rear cell (PERC) modules that are produced under comparable conditions. "Hidden contaminants" are not deliberately introduced, and their presence is typically only evident after accelerated testing. After 1000 h of DH testing, both TOPCon and HJT cells displayed a high significant sensitivity to "hidden contaminants", resulting in relative power losses of 10–16 %. Elemental analysis identified sodium (Na), calcium (Ca), magnesium (Mg), chlorine (Cl), and sulphur (S) as likely contributors. These contaminants are hypothesised to originate from (improper) handling during cell or module processing, such as contact with contaminated gloves, cassettes, packaging, or vacuum grippers. Under damp heat testing conditions, ions such as Na^{+}, Ca^{2+}, Mg^{2+}, Cl^{-}, and S^{2-} are likely to chemically react with moisture as well as with the passivation layers and/or metal contacts of solar cells. These reactions promote carrier recombination and induce corrosion of the metal contacts, ultimately degrading device performance. To minimise these effects, thorough deionised water cleaning, strict adherence to handling protocols using uncontaminated gloves, cassettes, packaging material, or vacuum grippers, and the exclusive use of clean stages prior to encapsulation are strongly recommended. These findings underscore the relatively high sensitivity of TOPCon and HJT solar cells and thus place critical importance on stringent contamination control to prevent unexpected failure in the field, in particular for module manufacturers with a range of solar cell suppliers.

1. Introduction

One of the primary strategies for reducing the levelized cost of electricity in photovoltaic (PV) systems is to ensure long-term module reliability, ideally over 25 years and preferably extending toward 50 years with no more than 20 % performance loss [1]. Silicon Passivated Emitter and Rear Cell (PERC) technology has been the dominant photovoltaic (PV) technology in the market since 2015 [2]. Meanwhile, tunnel oxide passivated contact (TOPCon) dominates the current market and heterojunction (HJT) solar cells are expected to rapidly gain market share due to their superior efficiencies [3]. HJT and TOPCon architectures have demonstrated record-breaking conversion efficiencies of up to 27.4 % for heterojunction interdigitated back-contact (HBC) cells and 26.58 % for industrial TOPCon cells [4,5]. Despite these achievements, HJT and TOPCon cells face critical reliability challenges when encapsulated using front-glass and rear-backsheet configurations, particularly under highly humid conditions [6–12]. To overcome these challenges, several cell-level strategies have been proposed, including the incorporation of SiN_x/SiO_x stack layers, AlO_x capping layers, the elimination of aluminum additives from silver paste, modifications to the contact formation process, and the adoption of copper plating as a barrier layer [13–16]. The vast majority of the manufacturers use polyolefin elastomer (POE)-based encapsulants and glass-glass module designs to mitigate moisture ingress. While these solutions enhance durability,

* Corresponding author.
** Corresponding author.
E-mail addresses: Chandany.sen@unsw.edu.au (C. Sen), b.hoex@unsw.edu.au (B. Hoex).

https://doi.org/10.1016/j.solmat.2025.113695
Received 3 February 2025; Received in revised form 31 March 2025; Accepted 6 May 2025
Available online 8 May 2025

they also introduce higher weight, increased breakage risks, and elevated costs [9,17–19]. As a result, front-glass/rear-backsheet modules remain the preferred choice for many applications, especially rooftop PV installations. Under high humid conditions, HJT-based modules frequently exhibit greater recombination losses, evident in reduced open-circuit voltage (V_{OC}), short-circuit current (J_{SC}), and fill factor (FF) [8,12,17,20,21] whereas TOPCon-based modules suffer increased series resistance (R_s) [9,10,19] leading to overall performance degradation. Such failures are often attributed to moisture ingress, which facilitates contamination-driven degradation [8,9,12,20]. Sodium (Na) and chloride (Cl) ions are somehow detected in failed regions of PV modules exposed to high humidity or prolonged field deployment, suggesting their critical role in failure mechanisms [22,23]. Na, for instance, can be released from solar glass under elevated voltage or leach due to moisture transport in the module, causing recombination losses in cells [8,12,24]. The source of Cl, however, remains unclear, warranting further investigation into its role in accelerating degradation processes.

In this study, we aim to reveal how improper handling practices, such as using contaminated gloves, cassettes, packaging material, or vacuum grippers can introduce, critical contaminants (Na, Ca, Mg, Cl, and S) that significantly exacerbate humidity-driven degradation in HJT and TOPCon modules, while we found PERC modules to be unaffected. These contaminants accumulate on cell surfaces or staging areas before encapsulation and, under damp heat conditions, interact with passivation layers, cell metallisation, and in the case of HJT, also with the transparent conductive oxide (TCO), and amorphous/microcrystalline silicon layers. As a result, the series resistance and recombination can increase, resulting in an efficiency loss. These findings underscore the need for strict contamination control of both manual and automated handling tools, especially for advanced cell architectures like HJT and TOPCon, which are significantly more sensitive to contamination than conventional PERC cells. To address this issue, we also propose a rapid, straightforward mitigation strategy to effectively minimise contamination-induced failure.

2. Methodology

In this study, bifacial n-type silicon HJT, TOPCon, and p-type PERC solar cells, sourced from industry and manufactured between 2019 (HJT and some PERC cells), 2023 (TOPCon and some PERC cells), and 2024 (some PERC cells) were used. The HJT cells incorporated intrinsic hydrogenated amorphous silicon (i-a-Si:H) passivation layers on both sides, complemented by phosphorus-doped (n-a-Si:H) and boron-doped (p-a-Si:H) hydrogenated amorphous silicon layers on the front and rear surfaces, respectively. Both sides featured indium tin oxide (ITO) layers with a screen-printed H-pattern silver grid. The PERC cells consisted of a phosphorus-doped emitter (n^+ emitter), a hydrogenated silicon nitride (SiN_x:H) passivation layer, and a screen-printed H-pattern silver grid on the front. The rear side included an aluminum oxide (Al_2O_3)/SiN_x:H passivation stack and a screen-printed H-pattern aluminum/silver grid. The TOPCon cells featured a boron-doped emitter (p^+ emitter) with a SiO_2/Al_2O_3/SiN_x:H passivation stack and a screen-printed H-pattern silver/aluminum grid on the front. The rear incorporated SiO_2/phosphorus-doped polysilicon (n^+ poly-Si)/SiN_x:H stack and a screen-printed H-pattern silver grid. A detailed schematic of HJT, PERC and TOPCon cell structures are depicted in Fig. 1. All solar cells were categorized into two groups: (1) encapsulated cells, referred to as modules, and (2) non-encapsulated cells. Group 1 cells were encapsulated by soldering interconnected ribbons and tabbing wires on both the front and rear sides. For PERC (Module A-H) and HJT modules (Modules A and B), encapsulation was performed using single-cell configurations, whereas TOPCon modules (Modules A and B) and PERC Module B-T featured series strings of 8–10 cells. The encapsulation layers for PERC and HJT cells consisted of Ethylene Vinyl Acetate (EVA) layers on both sides, sandwiched between a front glass sheet and a polymer backsheet. In contrast, TOPCon cells used POE layers with a similar configuration. The encapsulation process, including soldering and lamination, was carried out on industrial production lines at two separate facilities: one for HJT modules and another for TOPCon modules. PERC Module A-H was fabricated at the HJT facility, while PERC Module B-T was produced at the same facility as the TOPCon modules. For the HJT modules, a total of 16 samples were fabricated by Manufacturer A. In the case of the PERC modules, six samples were produced by Manufacturer A and Manufacturer B. For the TOPCon modules, 11 samples were fabricated by Manufacturer B. It is important to note that, for clarity and conciseness in presenting the results, only representative samples exhibiting the most pronounced localised failures, as well as those demonstrating no localised failures, were selected for demonstration. This approach is intended to avoid the repetition of similar data while effectively illustrating the phenomenon under investigation.

Group 2 cells (non-encapsulated) were further categorized into two subgroups: Subgroup 2-a: Uncleaned cells, which included TOPCon, HJT and PERC types, were handled with nitrile gloves that had previously

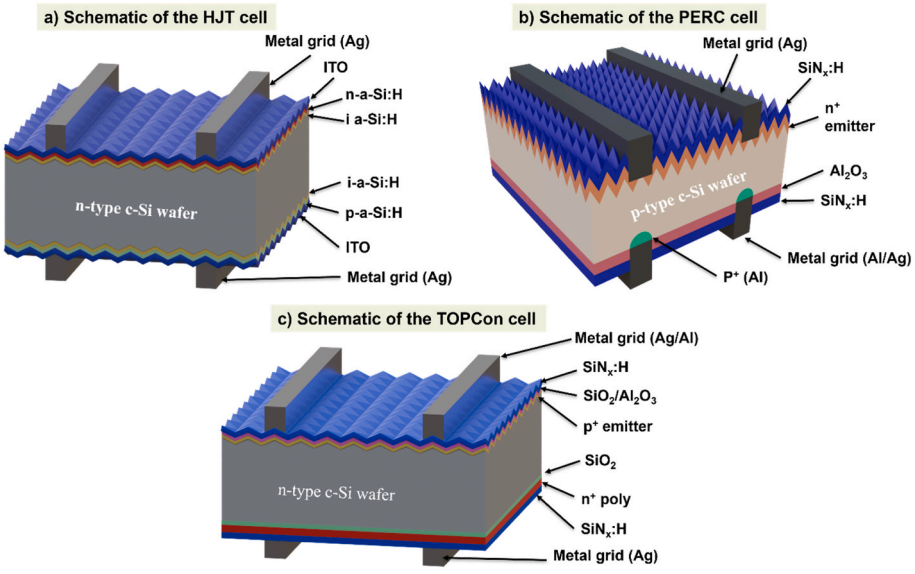

Fig. 1. Detailed schematic diagrams of (a) HJT cells, (b) PERC cells, and (c) TOPCon cells.

encountered various surfaces in the laboratory. These cells were also placed on the characterisation tools without any prior cleaning. Subgroup 2-b: Cleaned cells, which were handled exclusively with fresh nitrile gloves, cleaned using deionised water (DIW), and dried with nitrogen (N_2) gas. This cleaning procedure was conducted after pre-characterization and immediately prior to DH testing. All modules (HJT, TOPCon, PERC) and non-encapsulated HJT cells were subjected to DH testing at 85 °C and 85 % relative humidity (RH) for up to 1000 h. However, the non-encapsulated TOPCon cells were tested for a maximum of 30 h, while non-encapsulated PERC cells were tested for up to 200 h. It is noted that a variable testing duration was applied to non-encapsulated cells, depending on the observed failure outcomes. While some cells required extended exposure to replicate degradation observed in modules, others exhibited similar degradation mechanisms within a shorter timeframe. The detailed experimental setup and mini-module configuration are shown in Fig. 2.

Pre- and post-damp heat (DH) analyses were conducted as follows. The I-V characteristics of all TOPCon and PERC Module B–T modules were measured under standard test conditions (25 °C, AM1.5G, 1000 W/m^2) using a commercial module flash tester (Eternalsun Spire, Spi-Sun Simulator™ 5600SLP Blue System). I-V measurements for HJT cells/modules and PERC Module A–H were performed under the same conditions using the LOANA tool from pv-tools, while TOPCon and PERC cells in Group 2 were tested with the FCT-650 I-V tester from Sinton Instruments. Different I-V testers were employed due to equipment availability at the time of experimentation. These three testers use different methods to extract series resistance (R_s). The LOANA tester applies multi-light methods; Sinton Instruments calculates R_s by comparing the voltage difference between the Suns-Voc and I-V curves at a specific current (applying Ohm's Law); and the Eternalsun Spire system utilises a four-terminal Kelvin probe measurement, then compares it to a Suns-Voc measurement to eliminate wiring resistance. The resulting voltage difference at a specified current is then used to compute R_s. The line scan photoluminescence (PL_{LS}) and electroluminescence (EL) images were captured using a BTi (PL-M1) luminescence imaging system before and after the DH test. Internal Quantum Efficiency (IQE) mapping was performed using the Light Beam Induced Current (LBIC) method, using a LOANA tool from pv-tools, which measures the local photocurrent generated when a focused light beam scans across the solar cell's surface. Scale calibration was conducted in a dedicated quantum efficiency (QE) analysing mode, ensuring that the measurement beam was precisely aligned and restricted to the LBIC spot size on the cell area. A small spot size was employed in the LOANA system to maximise spatial resolution. In addition, a bias light of 0.3 was applied to replicate real-world operating conditions. For this study, measurements were taken for some specific HJT modules and HJT solar cells. The modules measured approximately 100 mm in width by 89 mm in height, while the cells measured 157 mm by 157 mm. During scanning, the same scan speed of about 75 μm/s was used across all samples to ensure consistency in data collection. Note that due to technical constraints and slow scanning speeds, the measurement instrument occasionally produced errors when attempting to scan larger areas. Consequently, measurements on the HJT module were limited to smaller regions featuring highly localised issues to minimise errors and focus on areas of interest. By carefully selecting the measurement parameters (spot size, bias light, and scanning speed), the LBIC-based IQE mapping provided detailed spatial information on how the cell responds to specific wavelengths of light. This comprehensive view facilitated the detection of localised performance issues, defects, or other non-uniformities in the device, even under partial illumination conditions. Time-of-flight secondary ion mass spectrometry (ToF-SIMS) depth profiling was used to compare the elemental composition of failed and non-failed (fresh) regions of non-encapsulated cells. Measurements were performed using a 30 keV Bi^+ primary ion beam with a 500 eV O_2 sputtering source on an ION-TOF TOF.SIMS 5 instrument. Additionally, scanning electron microscopy (SEM) was conducted on selected samples using a Zeiss 550 Crossbeam FIB-SEM at an accelerating voltage of 5 kV. Energy-dispersive X-ray spectroscopy (EDS, Oxford Instruments) was used to identify chemical elements, with data analysed using the Aztec software package, focusing on K-shell evaluation [25].

3. Results and discussion

Table 1 shows the I-V parameters of PERC modules and non-encapsulated cells before and after DH testing. Fig. 3 shows the EL images of PERC modules and the PL_{LS} images of non-encapsulated PERC cells, alongside their relative changes in I-V parameters after 1000 h (PERC modules) and 200 h (non-encapsulated PERC cells) of DH testing. PERC Module A-H [Fig. 3(a–b)] was encapsulated at the same site as the HJT modules, while PERC Module B-T [Fig. 3(c–d)] was encapsulated at

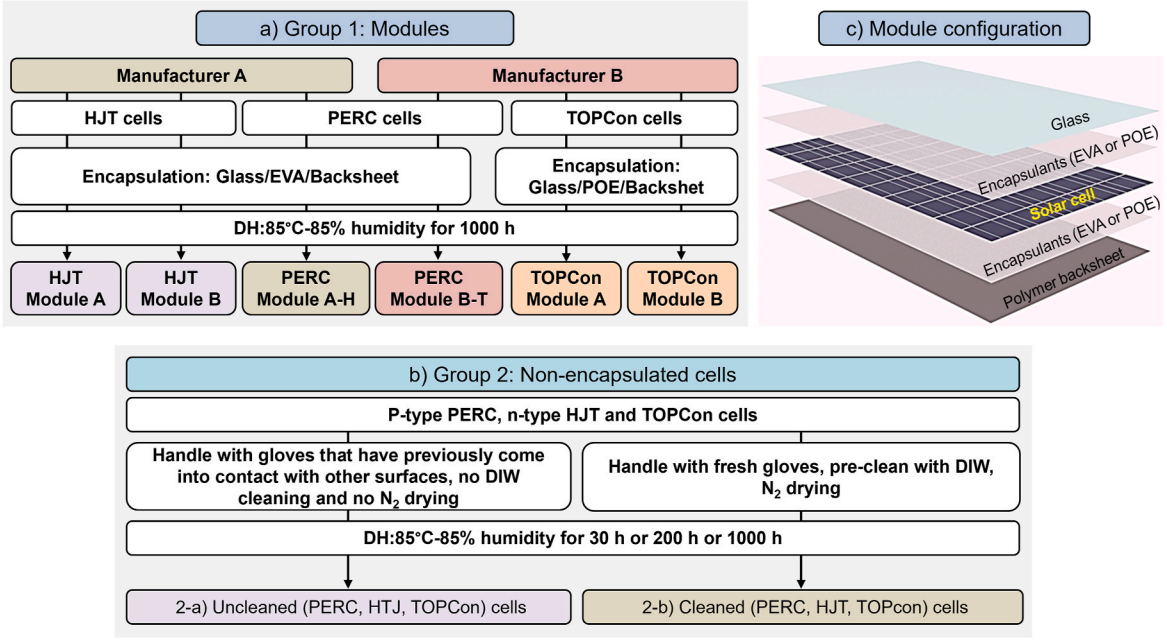

Fig. 2. Detailed experimental flow diagrams of (a) the module group, (b) the non-encapsulated cells group, and (c) the module configuration.

Table 1
Changes in I-V parameters of PERC modules and non-encapsulated cells before and after DH testing, including their corresponding relative changes after aging.

PERC Module A-H					
I-V parameters	P_{max} (W)	I_{SC} (mA)	V_{OC} (mV)	FF (%)	R_s (Ωcm^2)
Initial	3.81	7159	692	76.8	1.29
DH1000	3.82	7190	691	76.8	1.26
Relative changes ($\%_{rel}$)	**0.26**	**0.43**	**−0.14**	**0.00**	**−2.33**
PERC Module B-T					
I-V parameters	P_{max} (W)	I_{SC} (mA)	V_{OC} (mV)	FF (%)	R_s (Ω)
Initial	29.85	6758	5559	79.46	0.07
DH1000	29.54	6751	5569	78.57	0.08
Relative changes ($\%_{rel}$)	**−1.02**	**−0.10**	**0.19**	**−1.11**	**3.73**
Uncleaned PERC cell					
I-V parameters	P_{max} (W)	I_{SC} (mA)	V_{OC} (mV)	FF (%)	R_s (Ω)
Initial	7.88	13,839	699	81.439	0.0016
DH200	7.84	13,851	698	81.07	0.0017
Relative changes ($\%_{rel}$)	**−0.45**	**0.09**	**−0.01**	**−0.46**	**9.53**
Cleaned PERC cell					
I-V parameters	P_{max} (W)	I_{SC} (mA)	V_{OC} (mV)	FF (%)	R_s (Ω)
Initial	7.86	13,853	696	81.51	0.0015
DH200	7.83	13,837	696	81.32	0.0016
Relative changes ($\%_{rel}$)	**−0.37**	**−0.11**	**−0.04**	**−0.23**	**12.89**

the same site as the TOPCon modules. Both modules demonstrated stable performance, with no significant degradation observed in maximum power (P_{max}), fill factor (FF), open-circuit voltage (V_{OC}), or short-circuit current (I_{SC}). The P_{max} of PERC Module A–H remained effectively unchanged at 3.80 W before and after DH testing. PERC Module B–T showed only a minor relative decrease in P_{max} of ~1 $\%_{rel}$, from 29.85 W to 29.54 W. Changes in I_{SC}, V_{OC}, and FF were all within 1 $\%_{rel}$ or less. The series resistance (R_s) of both modules varied by only 2–4 $\%_{rel}$, which is relatively low compared to the TOPCon modules (discussed in a later section). Similarly, for the non-encapsulated PERC cells, both cleaned and uncleaned, the change in P_{max} after 200 h of DH testing was below 1 $\%_{rel}$. The variations in I_{SC} and V_{OC} were minimal, at a maximum of 0.1 $\%_{rel}$, and FF remained within 0.5 $\%_{rel}$. The R_s change was limited to approximately 13 $\%_{rel}$ for both cleaned and uncleaned samples. Note that slight variations in the absolute values of R_s, as well as differences in units, are due to the use of different I-V testers, as detailed in the methodology section. Furthermore, the EL images before and after DH testing showed no discernible differences, and no localised failures were observed [Fig. 3(a-d)]. Similarly, PL_{LS} images of both uncleaned and cleaned non-encapsulated PERC cells revealed no notable changes after 200 h of DH testing, with no evidence of localised point failures; see Fig. 3(e–h). These results indicate the intrinsic stability of PERC cells and suggest that they are less susceptible to humidity and contamination.

It is noted that, as outlined in the methodology section, PERC Module A-H was encapsulated at the same facility as the HJT module, using a similar configuration (front glass, EVA, and a polymer backsheet) with single cells per string. This design choice was made to enable direct comparisons with the HJT module. In contrast, PERC Module B-T was encapsulated at the same site as the TOPCon modules, with Manufacturer B using front glass, EVA, a polymer backsheet, and soldering methods consistent with the TOPCon encapsulation process. Both modules employed standard PERC cell architectures, as described in the methodology. PERC Module A-H was fabricated using half-cut cells (91 × 182 mm) from Manufacturer A, produced in approximately 2019, and assembled into a mini-module of about 200 × 200 mm. PERC Module B-T was made with half-cut cells of the same size from Manufacturer B, fabricated around 2023, and assembled into a larger module of approximately 400 × 400 mm comprising eight half-cells in a single string. Separately, non-encapsulated PERC cells (both cleaned and uncleaned) were sourced from yet another PV manufacturer in 2024, reflecting cell availability during the experiment. Despite these differences in manufacturer, production year, and module size, all PERC samples—both encapsulated and non-encapsulated—exhibited comparable electrical performance and no localised degradation following DH testing. This finding underscores the inherent stability of PERC cell technology across multiple suppliers and fabrication timelines.

Table 2 summarises the changes in I-V parameters for the HJT module and non-encapsulated HJT cells before and after 1000 h of DH testing, including their corresponding relative variations. After 1000 h of DH testing, both HJT Module B and the cleaned HJT cells (non-encapsulated) displayed minimal changes in their I-V parameters. The P_{max} experienced a decline of ~1–2 $\%_{rel}$, while V_{OC} and J_{SC} decreased by less than 1 $\%_{rel}$ after the testing period. In contrast, a significant loss in P_{max} was noted for HJT Module A and the uncleaned HJT cells. HJT Module A suffered degradation of ~10 $\%_{rel}$, whereas the uncleaned HJT cells recorded a more pronounced P_{max} loss of ~25 $\%_{rel}$. The main factors contributing to these losses were reductions in V_{OC} and J_{SC} with decreases in V_{OC} and J_{SC} of ~2 $\%_{rel}$, while the uncleaned HJT cells demonstrated a more substantial decline of ~7–8 $\%_{rel}$. No significant changes in R_s were observed across all samples. For Modules A and B, R_s improved by ~8 $\%_{rel}$. In non-encapsulated cells, R_s improved by 25 $\%_{rel}$ for the cleaned sample, while it remained nearly unchanged for the uncleaned cells. Consequently, the observed decrease in FF, ~14 % relative for the uncleaned cells and 6 % relative for HJT Module A, can be primarily attributed to increased and non-uniform recombination within the HJT cells, as evidenced by the PL_{LS} images in Fig. 4. Fig. 4 illustrates the evolution of line scan PL images for HJT modules and non-encapsulated cells before and after 1000 h of DH testing. The PL_{LS} images of HJT Module B and the cleaned cells, taken before and after the testing, appear quite similar, which aligns with the I-V results and indicates minimal changes in these samples post-DH test. However, numerous localised point failures were detected in HJT Module A and the uncleaned cells after 1000 h of DH testing, resulting in a decrease in PL_{LS} intensity. These observations align well with the observed reductions in V_{OC} and J_{SC} after the DH test. Note that the darker regions observed at the edges of the HJT module and the uncleaned HJT cell in Fig. 4 are attributed to localised degradation caused by contamination during handling. Specifically, gloves that had previously been used to handle other laboratory equipment unintentionally transferred foreign substances to the cell edges. These contaminants triggered chemical reactions that led to performance degradation in those areas following damp heat testing. It is important to note that although the HJT cells used in this study were fabricated around 2019, more recent HJT cells (produced around 2023–2024) have been found to be even more sensitive than those examined here. This increased sensitivity is likely due to modifications in the amorphous silicon and/or ITO layers (data not shown). These observations highlight the high sensitivity of HJT cells to surface contamination, particularly under high humidity conditions.

It should also be noted that HJT Modules A and B were both fabricated using a standard HJT cell with the architecture described in the Methods section and then encapsulated by Manufacturer A using a identical process. Specifically, both modules were packaged using front glass, EVA, and a polymer backsheet, each with a single cell per string. However, after DH testing, Module A exhibited localised degradation, while Module B did not. This difference is likely attributable to contamination introduced during handling prior to encapsulation for Module A—such as from unclean gloves, handling tools, or exposure to contaminated characterisation stages. In the presence of moisture during DH testing, this contamination could have led to increased recombination losses. In contrast, HJT Module B was likely handled using

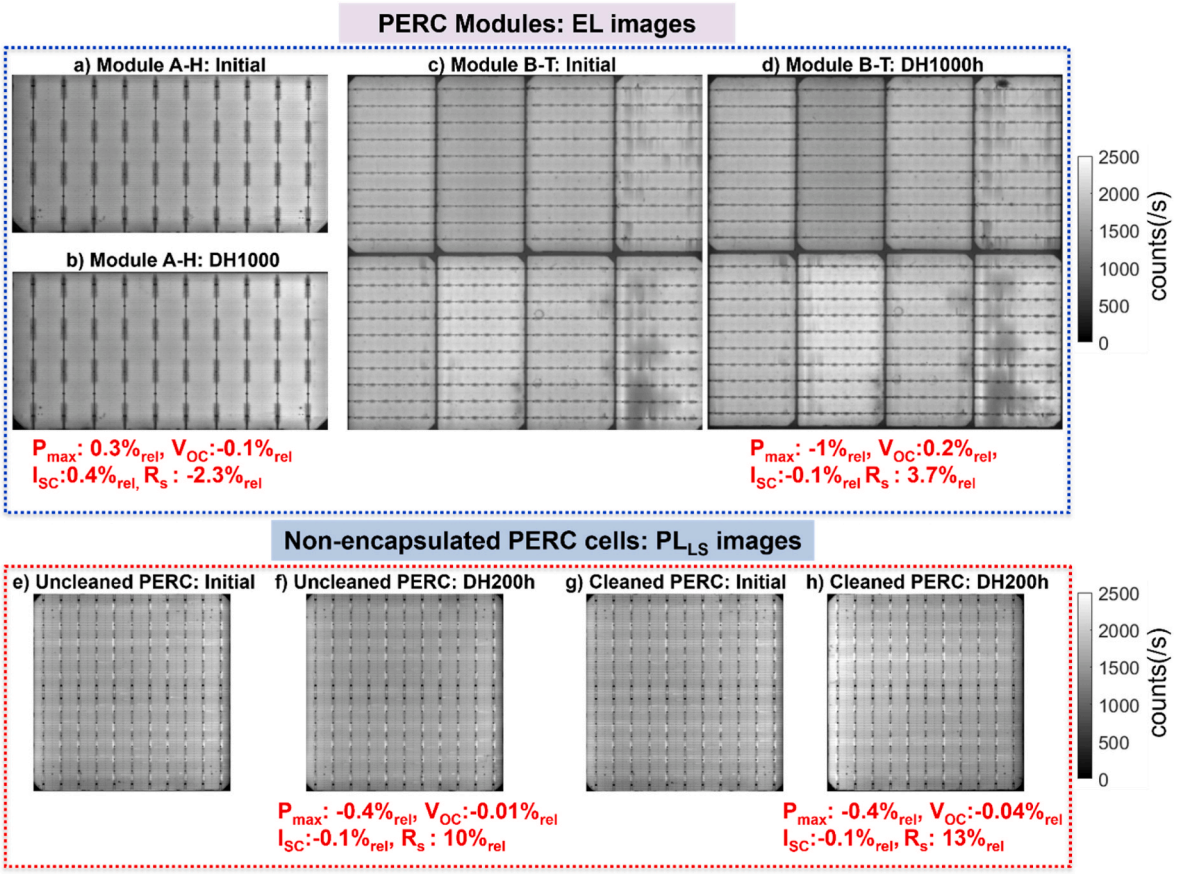

Fig. 3. EL images of PERC modules and non-encapsulated cells before and after DH testing. Images (a) and (b) correspond to EL images of Module A-H before and after 1000 h of DH testing, respectively. (c) and (d) EL images of Module B-T before and after 1000 h of DH testing. Images (e) and (f) depict the PL_{LS} of a non-encapsulated, uncleaned PERC cell in its initial state and after 200 h of DH testing, respectively. Similarly, images (g) and (h) show the PL_{LS} of a non-encapsulated, cleaned PERC cell in its initial state and after 200 h of DH testing. Relative changes in key performance metrics, including P_{max}, V_{OC}, $I_{SC,\ and}$ R_s, are also presented. Note: A negative value (−) indicates a decrease.

clean gloves and tools and may not have been exposed to contaminated environments prior to encapsulation. As a result, no significant localised degradation was observed following the DH testing.

Table 3 summarises the changes in I-V parameters for the TOPCon module and non-encapsulated TOPCon cells before and after DH testing, 1000 h for the module group and 30 h for the non-encapsulated cells, along with their corresponding relative variations. Fig. 5(a) illustrates the changes in EL images before and after 1000 h of DH testing. Consistent with the stability observed in HJT Modules, TOPCon Module B showed no significant reduction in P_{max}, V_{OC}, I_{SC} or increase in R_s with EL images remaining essentially unchanged before and after the DH test. In contrast, TOPCon Module A exhibited a ~15.6 $\%_{rel}$ drop in P_{max} (from ~30 W to 25.3W), attributed to a ~41 $\%_{rel}$ increase in R_s (from 0.07 Ω to 0.1 Ω). Pre-existing localised issues in Module A, visible as dark spots with low EL intensity in the initial images, became more pronounced after DH testing, further indicating increased R_s. Note that these localised dark EL regions in Module A corresponded to bright spots in PL_{LS} images (data not shown). Despite these localised changes, no significant variations in V_{OC} or J_{SC} were observed, with both parameters changing by less than 1 $\%_{rel}$, suggesting that the dark spots were primarily driven by the R_s increase. Fig. 5(b) presents PL_{LS} images of non-encapsulated TOPCon cells and the PL_{LS} ratio images, calculated by dividing the post-DH image by the pre-DH image. Cells handled with nitrile gloves previously exposed to other surfaces e.g., for I-V measurements (uncleaned TOPCon cell) exhibited a localised increase in PL_{LS} intensity in the touched areas, accompanied by a ~2.2 $\%_{rel}$ drop in P_{max} (from 7.9 W to 7.7 W) and an ~86 $\%_{rel}$ increase in R_s (from 1.1 mΩ to 2.1 mΩ) after just 30 h of DH testing, while V_{OC} and I_{SC} remained largely unaffected. These touched regions appeared as dark spots in EL images, further supporting an R_s-related failure mechanism. In contrast, non-encapsulated TOPCon cells handled under clean conditions with fresh nitrile gloves and no direct contact on the cell surface (cleaned TOPCon cell) showed negligible changes after 30 h of DH testing, maintaining stable PL_{LS} intensity. Specifically, P_{max} changed by only ~0.4 $\%_{rel}$, the FF decreased by 0.6 %, and R_s increased by ~19 $\%_{rel}$. Collectively, these results highlight the critical role of proper handling procedures. The use of contaminated gloves or the placement of cells in unclean environments can lead to localised failures, as observed in both HJT and TOPCon modules prior to and during encapsulation.

It is important to emphasise that both TOPCon Module A and TOPCon Module B were fabricated from the same standard TOPCon cells (sourced from the same PV manufacturer) and followed the same overall configuration—front glass, POE, and a polymer backsheet. The cell architecture is described in detail in the methodology section. Both modules also employed the same soldering flux, ribbons/tabbing wires, and lamination parameters (time and temperature), differing only in the number of cell strings (eight for Module A and ten for Module B). The key distinction lies in their handling conditions. TOPCon Module A was handled using standard procedures similar to those employed in the fabrication of PERC modules, which are known to be intrinsically stable and less sensitive to contamination, as demonstrated in the preceding section. In contrast, TOPCon Module B was subjected to more stringent handling protocols prior to encapsulation, which included consistently using fresh gloves and regularly cleaning automated handling tools with

Table 2
Changes in I-V parameters of HJT modules and non-encapsulated cells before and after DH testing, including their corresponding relative changes after aging.

HJT Module A					
I-V parameters	P_{max} (W)	I_{SC} (mA)	V_{OC} (mV)	FF (%)	R_s (Ωcm^2)
Initial	3.83	6780	748	75.5	2.25
DH1000	3.42	6583	735	70.8	2.08
Relative changes ($\%_{rel}$)	**−10.72**	**−2.91**	**−1.74**	**−6.23**	**−7.56**
HJT Module B					
I-V parameters	P_{max} (W)	I_{SC} (mA)	V_{OC} (mV)	FF (%)	R_s (Ωcm^2)
Initial	3.81	6698	744	76.6	1.93
DH1000	3.76	6683	743	75.7	1.78
Relative changes ($\%_{rel}$)	**−1.44**	**−0.22**	**−0.13**	**−1.17**	**−7.77**
Uncleaned HJT cell					
I-V parameters	P_{max} (W)	I_{SC} (mA)	V_{OC} (mV)	FF (%)	R_s (Ωcm^2)
Initial	3.52	5890	744	80.25	1.14105
DH1000	2.66	5512	686.5	69.4	1.1495
Relative changes ($\%_{rel}$)	**−24.55**	**−6.42**	**−7.73**	**−13.52**	**0.74**
Cleaned HJT cell					
I-V parameters	P_{max} (W)	I_{SC} (mA)	V_{OC} (mV)	FF (%)	R_s (Ωcm^2)
initial	3.26	5326	742	82.60	0.77
DH1000	3.20	5292	739	81.70	0.58
Relative changes ($\%_{rel}$)	**−2.03**	**−0.63**	**−0.40**	**−1.09**	**−24.59**

isopropanol (IPA) and DI water, then drying them with nitrogen gas. These measures were implemented to minimise contamination and ensure higher-quality sample handling.

To distinguish between surface and bulk recombination processes in the silicon wafer, IQE mapping was performed at 405 nm and 950 nm excitation wavelengths. This strategic selection leverages silicon's wavelength-dependent absorption coefficient: at 405 nm, the relatively high absorption confines photon penetration to the near-surface region, making IQE measurements especially sensitive to surface defects and contamination [26]. In contrast, 940 nm light penetrates deeper, providing insights into bulk and rear surface recombination [26]. A comparative analysis of IQE maps acquired at these two wavelengths highlights the evolution of recombination losses, showing how initial surface contamination observed at 405 nm transitions into bulk-dominated losses after 1000 h of DH testing.

To further determine whether the power loss in HJT cells originated from surface or bulk degradation, detailed IQE mapping was performed on degraded regions of both encapsulated modules and non-encapsulated cells, using both short (405 nm) and long (940 nm) wavelength excitation. Fig. 6(a–d) presents the PL_{LS} images of HJT Module A (same region where IQE was measured) before and after 1000 h of DH testing, as well as PL_{LS} images of an uncleaned HJT cell (from a new batch) before and after 200 h of DH testing. The PL_{LS} images are presented to emphasise localised failure areas, which are indicated by

Table 3
Changes in I-V parameters of TOPCon modules and non-encapsulated cells before and after DH testing, including their corresponding relative changes after aging.

TOPCon Module A					
I-V parameters	P_{max} (W)	I_{SC} (mA)	V_{OC} (mV)	FF (%)	R_s (Ω)
Initial	29.99	5.77	6706	77.56	0.07
DH1000	25.30	5.76	6655	65.98	0.10
Relative changes ($\%_{rel}$)	**−15.61**	**−0.05**	**−0.76**	**−14.93**	**40.66**
TOPCon Module B					
I-V parameters	P_{max} (W)	I_{SC} (mA)	V_{OC} (mV)	FF (%)	R_s (Ω)
Initial	38.53	7.30	6634	79.58	0.10
DH1000	38.51	7.28	6661	79.37	0.10
Relative changes ($\%_{rel}$)	**−0.03**	**−0.17**	**0.40**	**−0.26**	**2.31**
Uncleaned TOCon cell					
I-V parameters	P_{max} (W)	I_{SC} (mA)	V_{OC} (mV)	FF (%)	R_s (Ω)
Initial	7.90	13.26	718	82.94	0.0011
DH30	7.73	13.24	719	81.23	0.0021
Relative changes ($\%_{rel}$)	**−2.17**	**−0.15**	**0.05**	**−2.06**	**87.27**
Cleaned TOPCon cell					
I-V parameters	P_{max} (W)	I_{SC} (mA)	V_{OC} (mV)	FF (%)	R_s (Ω)
Initial	7.85	13.21	718	82.79	0.0013
DH30	7.82	13.23	719	82.30	0.0015
Relative changes ($\%_{rel}$)	**−0.36**	**0.18**	**0.06**	**−0.59**	**19.13**

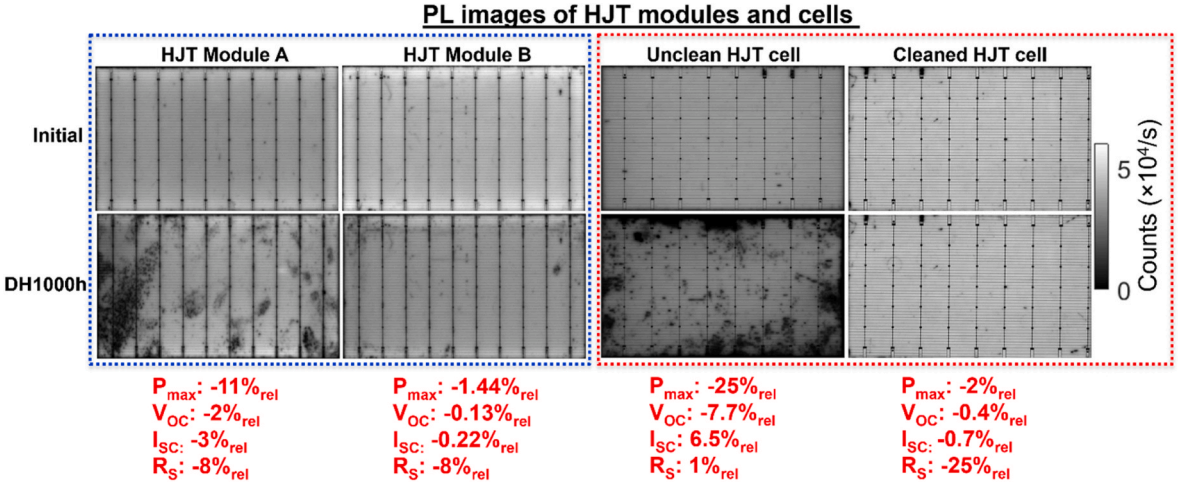

Fig. 4. PL_{LS} images of HJT modules and non-encapsulated cells before and after 1000 h of DH testing, along with the relative changes in key performance metrics, including P_{max}, V_{OC}, I_{SC}, and R_s. Note: Negative values (−) indicate a decrease, while positive values (+) indicate an increase.

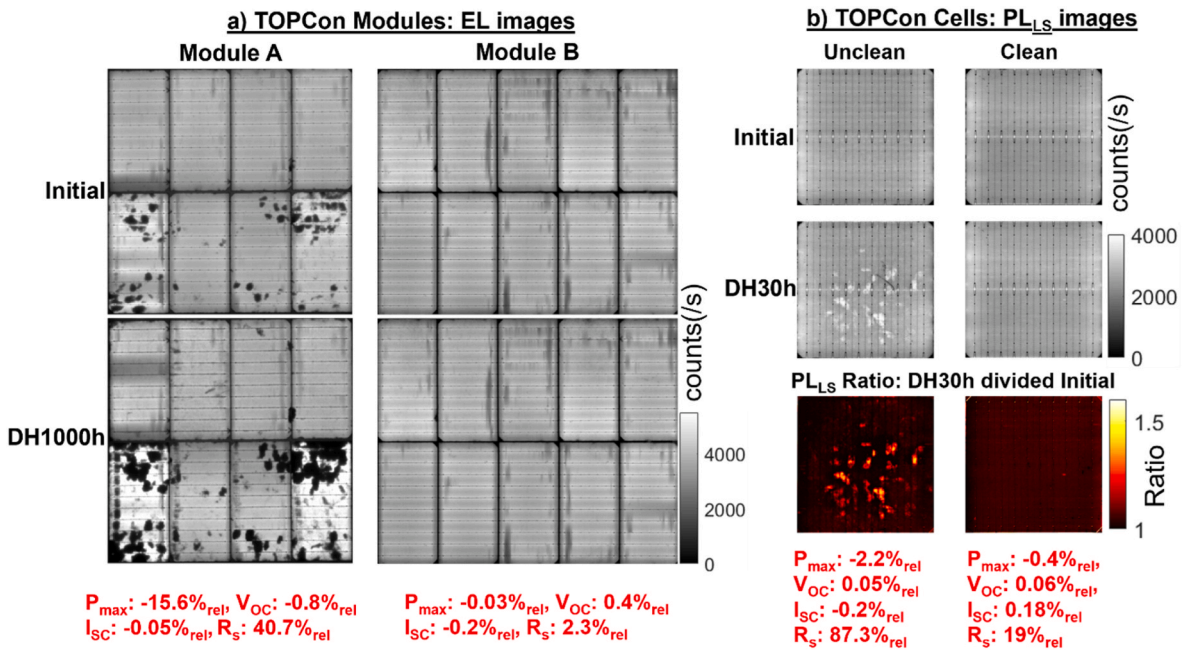

Fig. 5. (a) EL images of TOPCon modules captured before and after 1000 h of DH testing, along with the relative changes in P_{max}, V_{OC}, I_{SC}, and R_s after 1000 h of DH testing. (b) PL_{LS} images of non-encapsulated TOPCon cells taken before and after 30 h of DH testing, accompanied by the PL_{LS} ratio image, highlight the localised increase in R_s caused by prior contact with nitrile gloves contaminated from handling other materials. Relative changes in P_{max}, V_{OC}, I_{SC}, and R_s after 30 h of DH testing are also shown. Note: Negative values (−) indicate a decrease, while positive values (+) indicate an increase.

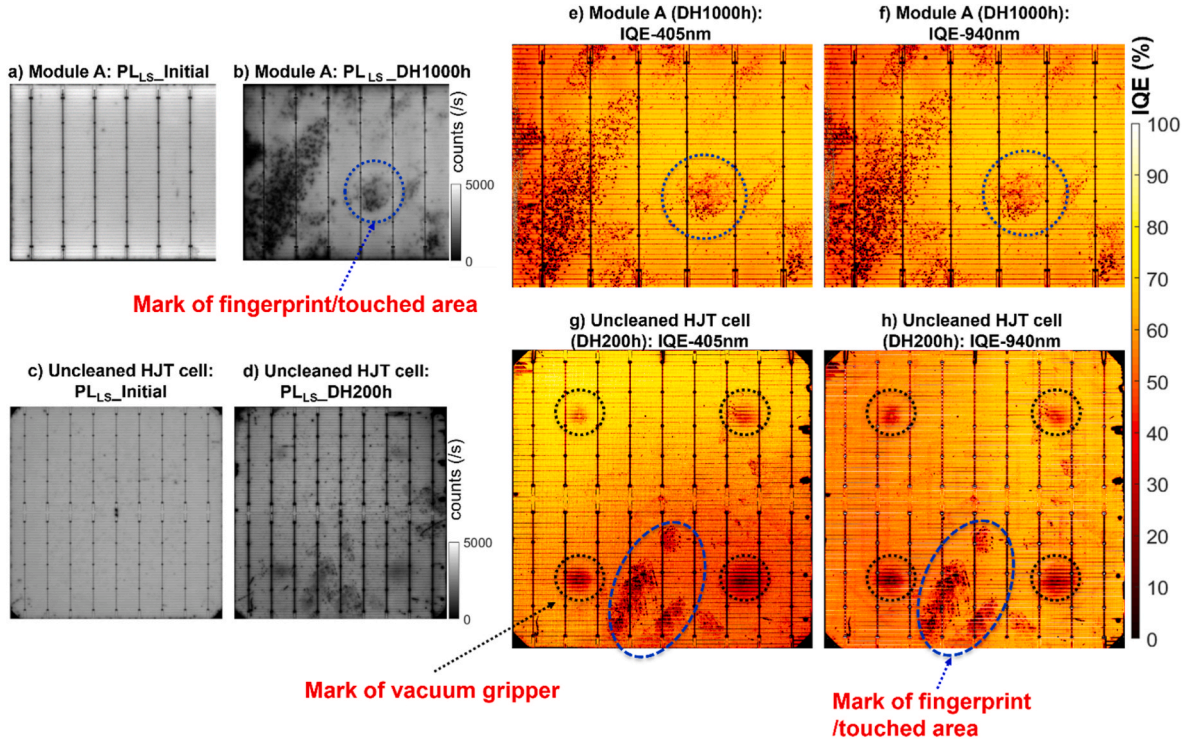

Fig. 6. PL_{LS} images of HJT Module A (a) before and (b) after 1000 h of DH testing, and PL_{LS} images of uncleaned, non-encapsulated HJT cells (c) before and (d) after 200 h of DH testing. IQE mapping of HJT Module A after 1000 h of DH testing at (e) 405 nm and (f) 940 nm. IQE mapping of the uncleaned HJT cell after ~200 h of DH testing at (g) 405 nm and (h) 940 nm.

reduced PL_{LS} intensity following DH testing, along with the corresponding IQE maps at both short and long wavelengths [Fig. 6(e–h)]. The IQE analysis on the failed modules [Fig. 6(e and f)] focused on the same HJT module (Module A) already shown in Fig. 4(b), covering roughly half of the module area. In contrast, the PL_{LS} and IQE analyses for the non-encapsulated HJT cells [Fig. 6 (c, d, g, h)] came from a different batch than those presented in Fig. 4(b). This separate batch exhibited a distinct failure pattern attributed to improper handling on an automated PV production line, specifically involving contact with a vacuum gripper. As shown in Fig. 6(a–d), the fresh HJT Module A and

uncleaned HJT cells appeared free of localised defects (i.e., "clean") prior to the DH test. However, after 1000 h of DH testing for the module and 200 h for the non-encapsulated cell, localised failure patterns emerged in the form of reduced PL_{LS} intensity. Notably, the uncleaned HJT cells were subjected to DH testing (85 °C and 85 % RH for ~200 h) at the PV manufacturer's facility, but the characterisation of IQE mapping images was done at UNSW. In both the 405 nm and 940 nm IQE mappings, as well as in the PL_{LS} images, the failed regions in HJT Module A and the uncleaned HJT cell displayed similar "fingerprint" patterns [blue dashed lines in Fig. 6(b–e, f, g, h)]. Additionally, vacuum gripper marks were visible on the uncleaned cell at both short and long wavelengths [black dashed lines in Fig. 6(g and h)], leading to a reduced IQE. The presence of identical failure patterns in both short- and long-wavelength IQE mappings suggests that degradation occurs at the front surface and within the silicon bulk of HJT cells. IQE measures how efficiently charge carriers are collected after photon absorption [26]. Local decreases in IQE indicate increased recombination at defects, reducing carrier density, quasi-Fermi level splitting, and thus V_{OC}. Proportional drops in IQE and external quantum efficiency (EQE) also lower I_{SC} by limiting photogenerated carriers [26]. Contamination from "fingerprints" (likely from nitrile gloves) and vacuum gripper residues may react with moisture, ITO, and the a-Si stack, forming recombination centers that hinder carrier collection. Consequently, both V_{OC} and I_{SC} decrease, lowering HJT cell power output, as shown in Fig. 4.

To identify the specific contaminants contributing to the observed failure, TOF-SIMS depth profiling was performed on both the failed region of an uncleaned HJT cell (after ~200 h of DH testing) and on a fresh HJT cell that had not undergone DH testing. The TOF-SIMS results are presented in Fig. 7. These TOF-SIMs results indicate that in the fresh HJT cell, sodium (Na^+) and calcium (Ca^{2+}) ion signals remained below 10^2 counts, even after sputtering longer than 3500 s. In contrast, the failed region of the uncleaned HJT cell exhibited significantly elevated Na^+ and Ca^{2+} signals. Specifically, the intensities reached ~10^5 counts at the surface, remained at ~10^4 counts within the doped layer (observed during ~500–1000 s of sputtering), and gradually decreased to ~4 × 10^3 counts in the silicon bulk (>1000 s of sputtering). It is essential to note that while these results strongly indicate a correlation between Na^+/Ca^{2+} contamination and cell failure, the origin of the observed signals in deeper regions remains ambiguous. Specifically, it is unclear whether the ions (Na^+/Ca^{2+}) originated from the bulk silicon or resulted from residual surface contamination redistributed during sputtering, an artifact in SIMS analysis due to incomplete removal of surface layers or ion mixing [27,28]. Nonetheless, these findings imply that Na^+ and Ca^{2+} contaminants may contribute to the degradation of HJT cells, potentially by compromising the quality of the amorphous silicon passivation layers. Under damp heat testing conditions, it is likely that these ions react chemically with moisture and the passivation layers of the HJT cells, thereby introducing recombination centers that reduce both the V_{OC} and the I_{SC}. Consistent with the short- and long-wavelength IQE data, this mechanism explains the observed decrease in cell performance.

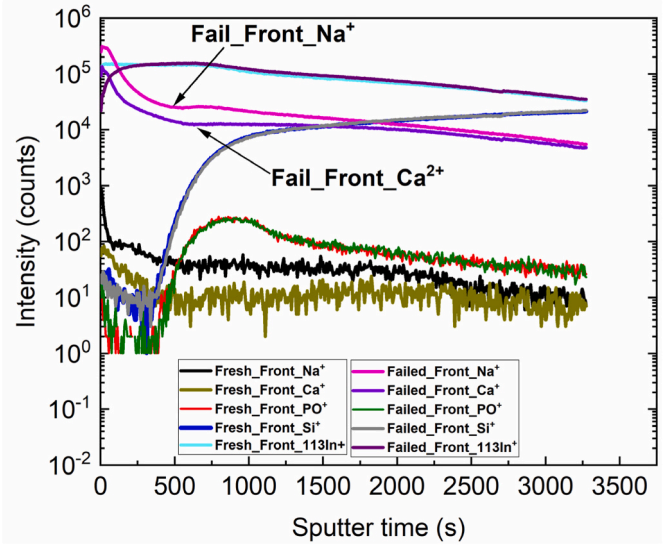

Fig. 7. TOF-SIMS depth profiling on the failed region of the uncleaned HJT cell that underwent 200 h of DH testing and the fresh cell that did not undergo DH testing. Fresh_Front represents the front side of the fresh cell and Fail_Front represents the front side of the uncleaned cell (failed region).

It is important to note that due to the textured surface of the HJT cells used in this study, the correlation between detected ion intensities (e.g., Na^+, Ca^+) and actual sputtering depth is less reliable. According to the principles of ToF-SIMS, determining absolute sputter depth on rough or textured surfaces is inherently uncertain due to factors such as uneven crater formation, variable sputter yields, shadowing effects, and redeposition of material [29]. Although sputter rates can be estimated using calibrations on polished silicon wafers—for example, ~0.1 nm/s under 500 eV, 100 nA O_2^+ ion beam conditions in our case—these values do not directly translate to textured surfaces, where local sputtering behavior can vary significantly. As such, while it is still informative to plot ion intensities versus nominal depth or sputtering time, the resulting depth scale should be interpreted as approximate. For textured samples like the HJT solar cells in this study, presenting ToF-SIMS results as ion intensity versus sputter time is a more rigorous and reliable approach. This method enables a meaningful comparison of elemental distribution trends across samples while acknowledging the semi-quantitative nature of depth profiling under these surface conditions.

Fig. 8 presents top-view SEM images, EDS mapping, point-spectrum analyses, and their corresponding weight percentages (wt%) for stable and failed regions on the front side of uncleaned TOPCon cells. The SEM image of the stable region [Fig. 8(a)] reveals a clean metal electrode surrounded by a uniform morphology, free from visible defects, irregularities, or contaminants. Elemental analysis shows that the passivation layer contains Si and N while Ag, Pb, Zn, and Al come from the Ag paste used for the front metal contact. O is present in both the passivation layer and the metal contact of TOPCon cells. The presence of carbon (C) is likely due to environmental contamination and/or the microscopy tool [30]. No Na, Ca, Mg, Cl, or S were detected in the stable regions. In contrast, the SEM image of the failed region shows visible contamination on and around the metal contact. Similar to HJT cells, Na (0.3–2.4 wt%) and Ca (1.6–5.5 wt%) were detected, alongside Cl (0.3–1.8 wt%), S (0.1–0.5 wt%), and minor amounts of Mg (0.05–1.6 wt%) in the failed regions of the TOPCon cell. Elements like O and Si originate from the passivation layer of TOPCon cells, whereas Ag and Pb come from the metal contact. C is again attributed to environmental contamination and/or the microscopy tool [30,31]. A low accelerating voltage (5 kV) was used during the EDS analysis to enhance the detection of surface contaminants, limiting the analysis depth to approximately 0.5 μm [31,32]. Consequently, if the contaminant layer on the surface is relatively thick or abundant, the primary electron beam may not penetrate deep enough to detect certain underlying cell elements. This effect is evident in P-1 of the failed regions, where Ag was not detected on the surface of the Ag electrode [31]. The presence of Na, Ca, Mg, Cl, and S in the failed areas may have induced chemical reactions with the metal contacts under damp heat test conditions, thereby increasing the R_s and contributing to the observed degradation in the TOPCon cells.

It is noted that for failed samples, point & ID EDS analysis was chosen over SEM-EDS mapping due to its proven effectiveness in detecting localised contamination on the samples [33]. By focusing on specific points, point & ID EDS provides precise quantitative measurements, making it particularly useful for identifying contaminants responsible for localised failures. In contrast, SEM-EDS mapping proved less effective for capturing small-scale contamination on the solar cell surface [33,34]. Several factors contributed to this limitation. First, the analyses

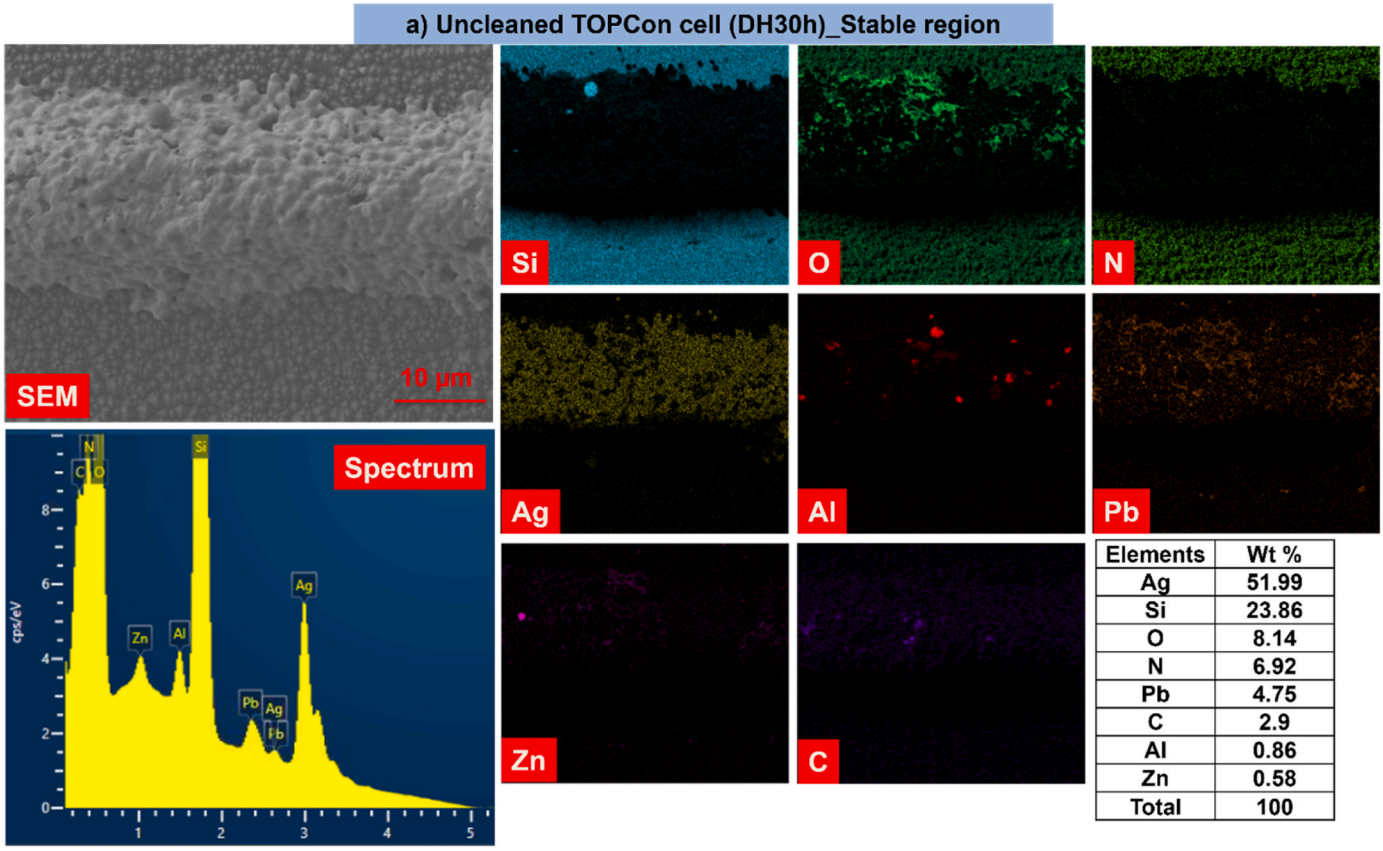

Elements	Wt %
Ag	51.99
Si	23.86
O	8.14
N	6.92
Pb	4.75
C	2.9
Al	0.86
Zn	0.58
Total	100

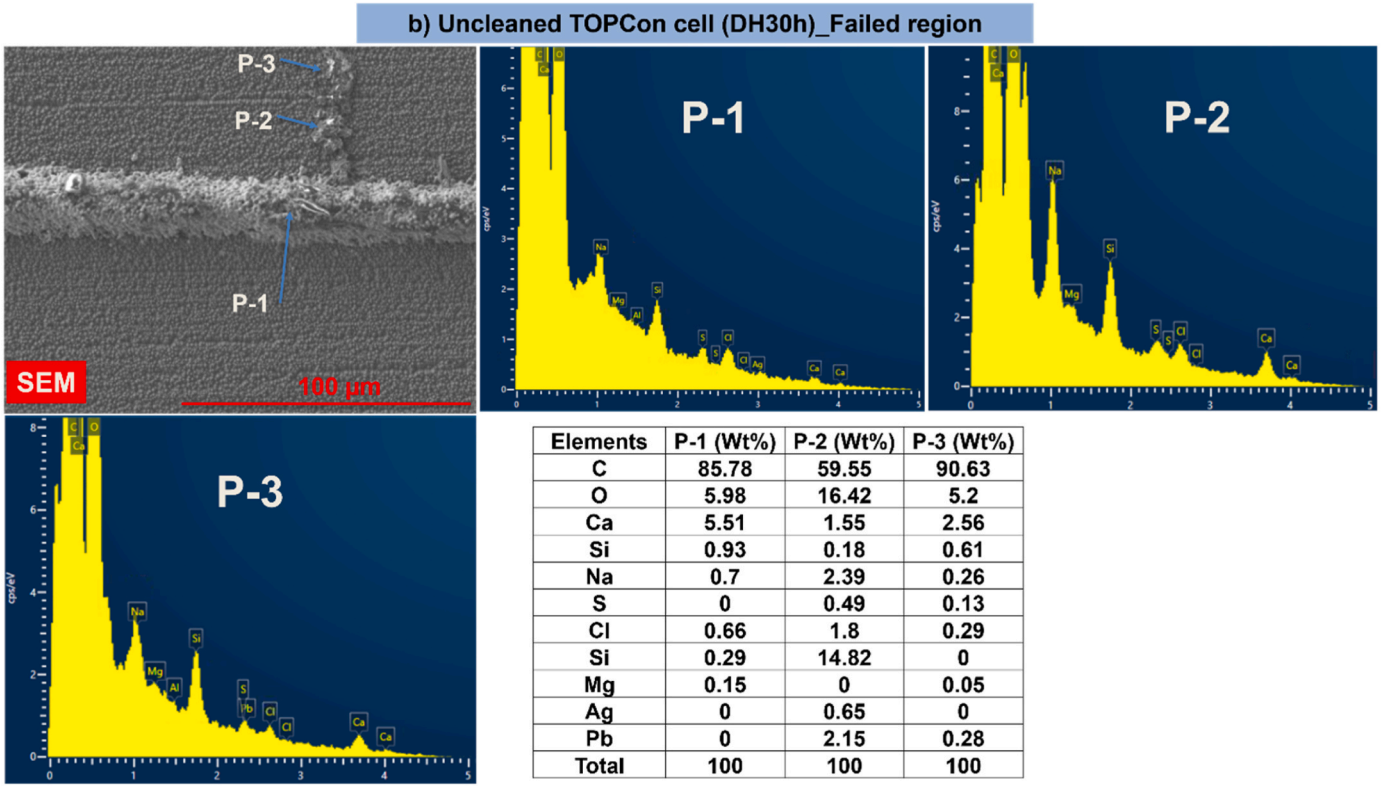

Elements	P-1 (Wt%)	P-2 (Wt%)	P-3 (Wt%)
C	85.78	59.55	90.63
O	5.98	16.42	5.2
Ca	5.51	1.55	2.56
Si	0.93	0.18	0.61
Na	0.7	2.39	0.26
S	0	0.49	0.13
Cl	0.66	1.8	0.29
Si	0.29	14.82	0
Mg	0.15	0	0.05
Ag	0	0.65	0
Pb	0	2.15	0.28
Total	100	100	100

Fig. 8. (a) Top-view SEM images, EDS mapping, and spectrum analyses of the stable region in uncleaned TOPCon cells. (b) Top-view SEM images, point EDS analysis, and elemental composition summary of the failed region in uncleaned TOPCon cells after 30 h of DH testing, revealing the presence of Na, Ca, Cl, S, and Mg in the degraded area.

were conducted at a lower accelerating voltage (5 kV) to reduce the electron interaction volume and enhance surface sensitivity, which is critical for detecting contaminants on thin surface layers [32,35]. Second, each sample was scanned for only around 10 min, a short duration that, when combined with the low accelerating voltage, lowered the signal-to-noise ratio—making trace element detection through mapping difficult [36]. Finally, because the contaminants occurred at low concentrations and in highly localised areas, mapping scans did not clearly reveal them. Given these constraints, point & ID EDS fulfils the analysis requirements by providing reliable, localised contamination data without depending on SEM-EDS mapping.

Recent studies have demonstrated that Na can substantially accelerate carrier recombination in HJT cells [8,12,37–39], leading to pronounced reductions in V_{OC}, J_{SC}, and thus, substantial power loss. Consistent with these findings, our previous work showed that exposure to NaCl caused a ~50–80 $\%_{rel}$ drop in P_{max} within only 20 h in non-encapsulated HJT and TOPCon cells; however, PERC cells remained largely unaffected under similar DH test conditions [40–42]. Further research confirms the presence of Na and Cl in failed regions of PV modules subjected to field exposure or indoor DH testing, highlighting the detrimental effect of these contaminants on device performance [22,23]. Notably, Na can be released from solar glass under high voltage conditions or leach from the glass as a result of moisture ingress, impairing cell performance through increased recombination losses [8,12,24,43,44]. However, the source of Cl is not understood at the moment.

Interestingly, in this study, PERC modules from two different manufacturers displayed no localised failures after DH testing. In contrast, the HJT (Modules A and B) and TOPCon (Modules A and B) modules, each fabricated at distinct production sites, showed significant performance discrepancies despite encapsulation under the same respective site conditions. Specifically, HJT Modules A and B were encapsulated at one facility, while TOPCon Modules A and B were encapsulated at another. PERC Module A-H was manufactured by the HJT-producing facility (Manufacturer A), and PERC Module B-T by the TOPCon-producing facility (Manufacturer B). Based on the DH test outcomes of non-encapsulated cells (Group 2 samples) and the detailed analysis using IQE mapping, SEM-ESD and TOF-SIMS, it is likely that Modules A and B experienced different handling procedures prior to encapsulation, resulting in varying levels of contamination (e.g., Na^+, or Ca^{2+} or Mg^{2+} or Cl^- or S^{2-}). These observations suggest that moisture by itself may not significantly degrade TOPCon and HJT cells, even when lower-cost encapsulants such as EVA are used. However, if cells are contaminated beforehand, severe degradation can occur despite using higher-quality encapsulants like POE. This conclusion is supported by the performance of cleaned HJT and TOPCon cells, which exhibited negligible degradation under comparable DH conditions, as well as by the robust behaviour of PERC cells, likely due to their inherent stability and lower sensitivity to such contaminants [40].

As detailed in the methodology section, this investigation involved the fabrication of HJT, PERC, and TOPCon photovoltaic modules to examine the occurrence of localised failure. For HJT modules, a total of six samples was fabricated by Manufacturer A in the first batch, of which five exhibited localised failure, similar to HJT Module A, though some samples varied in the extent of localised failure. One HJT module from this batch (HJT Module B) remained relatively stable. In contrast, a second batch of ten HJT modules fabricated using the same bill of materials showed no signs of localised failure, indicating a significant improvement in stability. For PERC modules, two samples were fabricated by Manufacturer A and four by Manufacturer B, all of which demonstrated consistent stability with no evidence of localised failure. In the case of the TOPCon modules, the first batch from Manufacturer B consisted of seven modules, all of which exhibited localised failure similar to TOPCon Module A, though varying in the extent of failure. However, a subsequent batch of four modules, fabricated using the same materials, displayed no localised failure. To enhance clarity and avoid redundancy, only representative samples demonstrating the most pronounced localised failures and those exhibiting no localised failures are presented, ensuring an effective illustration of the phenomenon under investigation. The statistical summary highlights that localised failure was predominantly associated with the initial batches of HJT and TOPCon modules, where both manufacturers were previously unaware of the detrimental impact of improper handling. Following this study's findings, subsequent batches fabricated under improved handling protocols exhibited significantly enhanced stability. The absence of localised failure in PERC modules across both manufacturers underscores the robustness of the fabrication process for this technology.

Our findings underscore the critical importance of stringent handling protocols in the manufacturing of both HJT and TOPCon, especially for PV manufacturers sourcing cells from external suppliers. To mitigate contamination risks and preserve cell performance, we recommend the following measures: "Cell handling" always use fresh, clean gloves, wafer cassettes, and packaging materials at every stage of cell handling. "Equipment maintenance" rigorously cleans all characterisation equipment prior to use. "Pre-encapsulation rinse": If there is any possibility that cells have been exposed to contaminated tools, rinse them with deionised water before encapsulation, then thoroughly dry them in an N_2 environment. Implementing these measures is essential for minimising surface contamination and ensuring optimal performance in both cell types.

4. Conclusion

This study demonstrates that "hidden contaminants" play a pivotal role in damp heat-induced degradation of HJT and TOPCon glass-backsheet modules, while PERC modules remain largely unaffected. After 1000 h of DH testing, HJT and TOPCon modules with potential prior contamination exhibited significant susceptibility, resulting in 10–16 % relative power losses. In HJT cells, these contaminants primarily increased recombination losses, whereas, in TOPCon cells, they manifested as higher series resistance, leading to reduced device performance. Elemental analyses identified Na, Ca, Mg, Cl, and S as likely contributors. We hypothesise that these contaminants are highly likely to originate from improper handling during cell or module processing, such as contact with unclean gloves, cassettes, packaging material, or vacuum grippers. Under damp heat test conditions, these ions, including Na^+, Ca^{2+}, Mg^{2+}, Cl^-, and S^{2-}, likely chemically react with moisture. This reaction may have promoted charge-carrier recombination (in HJT cells) and metal contact corrosion (in TOPCon cells), exacerbating performance degradation. To minimise these adverse effects, rigorous deionised water cleaning, strict adherence to contamination-free handling protocols, and the exclusive use of clean staging areas prior to encapsulation are strongly recommended. These findings underscore the importance of meticulous contamination control to avert unexpected failure modes in HJT and TOPCon technologies.

CRediT authorship contribution statement

Chandany Sen: Writing – review & editing, Writing – original draft, Visualization, Validation, Methodology, Investigation, Formal analysis, Data curation, Conceptualization. **Haoran Wang:** Methodology, Investigation, Data curation. **Muhammad Umair Khan:** Methodology, Investigation, Data curation. **Jiaxin Yang:** Methodology, Investigation. **Ziruo Zhu:** Investigation, Data curation. **Anjie Li:** Investigation, Data curation. **Bram Hoex:** Writing – review & editing, Validation, Supervision, Resources, Project administration, Conceptualization.

Declaration of competing interest

The authors declare that they have no known competing financial interests or personal relationships that could have appeared to influence the work reported in this paper.

Acknowledgment

This research was supported by theAustralian Government through the Australian Renewable Energy Agency (ARENA 1–060 Extension project), the Australian Centre for Advanced Photovoltaics (ACAP) funded by ARENA, and the Australian Government's Trailblazer for Recycling and Clean Energy (TRaCE) program, led by UNSW and the University of Newcastle. The authors acknowledge that the views, information, and advice expressed in this publication are solely their own and do not necessarily reflect those of the Australian Government. The authors extend their heartfelt thanks to Dr. Charlie Kong for his invaluable assistance and to the Electron Microscope Unit at UNSW for providing access to the ZEISS Cryogenic Focused Ion Beam (Cryo-FIB) instrument. Special acknowledgment is given to Dr. Bill Bin Gong and Dr. Songyan Yin for their expertise in conducting TOF-SIMS measurements on HTJ cells at the Surface Analysis Laboratory, SSEAU, MWAC, at UNSW. Finally, the authors express their sincere gratitude to the LDOT team at SPREE UNSW, based in TETB and SIRF, for their exceptional support in maintaining rigorous health and safety standards and ensuring the seamless operation of laboratory facilities, which were instrumental in the success of this research.

Data availability

Data will be made available on request.

References

[1] I.M. Peters, J. Hauch, C. Brabec, P. Sinha, The value of stability in photovoltaics, Joule 5 (2021) 3137–3153, https://doi.org/10.1016/j.joule.2021.10.019.
[2] M.A. Green, The passivated emitter and rear cell (PERC): from conception to mass production, Sol. Energy Mater. Sol. Cell. 143 (2015) 190–197, https://doi.org/10.1016/j.solmat.2015.06.055.
[3] International Technology Roadmap for Photovoltaics (ITRPV) 2023 Results, fifteenth ed., 2024.
[4] Solar Trina, TrinaSolar unveils i-TOPCon ultra technology, with cell efficiency of 26.58. https://static.trinasolar.com/en-apac/resources/newsroom/aptrinasolar-unveils-i-topcon-ultra-technology-cell-efficiency-2658, 2024. (Accessed 21 January 2025).
[5] M.A. Green, E.D. Dunlop, M. Yoshita, N. Kopidakis, K. Bothe, G. Siefer, D. Hinken, M. Rauer, J. Hohl-Ebinger, X. Hao, Solar cell efficiency tables (Version 64), Prog. Photovoltaics Res. Appl. 32 (2024) 425–441, https://doi.org/10.1002/pip.3831.
[6] C. Sen, H. Wang, X. Wu, M.U. Khan, C. Chan, M. Abbott, B. Hoex, Four failure modes in silicon heterojunction glass-backsheet modules, Sol. Energy Mater. Sol. Cell. 257 (2023) 112358, https://doi.org/10.1016/j.solmat.2023.112358.
[7] C. Sen, H. Wang, M.U. Khan, J. Fu, X. Wu, X. Wang, B. Hoex, Buyer aware? Three new failure modes in TOPCon modules absent from PERC technology, Sol. Energy Mater. Sol. Cell. (2024), https://doi.org/10.1016/j.solmat.2024.112877.
[8] L. Gnocchi, O.A. Arruti, C. Ballif, A. Virtuani, A comprehensive physical model for the sensitivity of silicon heterojunction photovoltaic modules to water ingress, Cell Rep. Phys. Sci. 5 (2024), https://doi.org/10.1016/j.xcrp.2023.101751.
[9] P.M. Sommeling, J. Liu, J.M. Kroon, Corrosion effects in bifacial crystalline silicon PV modules; interactions between metallization and encapsulation, Sol. Energy Mater. Sol. Cell. 256 (2023), https://doi.org/10.1016/j.solmat.2023.112321.
[10] C. Sen, H. Wang, M.U. Khan, J. Fu, X. Wu, X. Wang, B. Hoex, Buyer aware: three new failure modes in TOPCon modules absent from PERC technology, Sol. Energy Mater. Sol. Cell. 272 (2024), https://doi.org/10.1016/j.solmat.2024.112877.
[11] P. Gebhardt, U. Kräling, E. Fokuhl, I. Hädrich, D. Philipp, Reliability of commercial TOPCon PV modules—an extensive comparative study, Prog. Photovoltaics Res. Appl. (2024), https://doi.org/10.1002/pip.3868.
[12] L. Pirot-Berson, R. Couderc, R. Bodeux, J. Dupuis, Failure modes of silicon heterojunction photovoltaic modules in damp heat environment: sodium and moisture effects, Sol. Energy Mater. Sol. Cell. 278 (2024), https://doi.org/10.1016/j.solmat.2024.113190.
[13] W. Liu, L. Zhang, X. Yang, J. Shi, L. Yan, L. Xu, Z. Wu, R. Chen, J. Peng, J. Kang, K. Wang, F. Meng, S. De Wolf, Z. Liu, Damp-heat-stable, high-efficiency, industrial-size silicon heterojunction solar cells, Joule 4 (2020) 913–927, https://doi.org/10.1016/j.joule.2020.03.003.
[14] X. Wu, C. Sen, H. Wang, X. Wang, Y. Wu, M.U. Khan, L. Mao, F. Jiang, T. Xu, G. Zhang, B. Hoex, Addressing sodium ion-related degradation in SHJ cells by the application of nano-scale barrier layers, Sol. Energy Mater. Sol. Cell. 264 (2024) 112604, https://doi.org/10.1016/j.solmat.2023.112604.
[15] X. Wu, X. Wang, W. Yang, J. Nie, J. Yuan, M.U. Khan, A. Ciesla, C. Sen, Z. Qiao, B. Hoex, Enhancing the reliability of TOPCon technology by laser-enhanced contact firing, Sol. Energy Mater. Sol. Cell. 271 (2024), https://doi.org/10.1016/j.solmat.2024.112846.
[16] X. Wang, C. Sen, X. Wu, Y.-C. Chang, H. Wang, M.U. Khan, B. Hoex, Alleviating contaminant-induced degradation of TOPCon solar cells with copper plating, Sol. Energy Mater. Sol. Cell. 282 (2025) 113444, https://doi.org/10.1016/j.solmat.2025.113444.
[17] J. Karas, A. Sinha, V.S.P. Buddha, F. Li, F. Moghadam, G. Tamizhmani, S. Bowden, A. Augusto, Damp heat induced degradation of silicon heterojunction solar cells with Cu-plated contacts, IEEE J. Photovoltaics 10 (2020) 153–158, https://doi.org/10.1109/JPHOTOV.2019.2941693.
[18] M. Hutchins, The weekend read: bifacial drives PV encapsulant switch, Pv Magazine International (2021). https://www.pv-magazine.com/2021/03/20/the-weekend-read-bifacial-drives-pv-encapsulant-switch/. (Accessed 18 March 2024).
[19] Y. Zhou, D. Chen, Y. Ye, H. Yin, X. Niu, Damp-heat endurance investigation of PV modules based on n-type bifacial passivated contact cells, in: 40th European Photovoltaic Solar Energy Conference and Exhibition, 2023, https://doi.org/10.4229/EUPVSEC2023/3AV.2.41.
[20] J. Karas, B. Phua, A. Mo, N. Iqbal, K. Davis, S. Bowden, A. Lennon, A. Augusto, Copper outdiffusion from copper-plated solar cell contacts during damp heat exposure, ACS Appl. Mater. Interfaces (2021), https://doi.org/10.1021/acsami.1c21218.
[21] K. Zhang, O. Mashkov, M.A. Yaqin, B. Doll, A. Lambertz, K. Bittkau, W. Duan, I. M. Peters, C.J. Brabec, U. Rau, K. Ding, Damp-heat–induced degradation of lightweight silicon heterojunction solar modules with different transparent conductive oxide layers, Prog. Photovoltaics Res. Appl. (2025), https://doi.org/10.1002/pip.3880.
[22] S. Kumar, R. Meena, R. Gupta, Imaging and micro-structural characterization of moisture induced degradation in crystalline silicon photovoltaic modules, Sol. Energy 194 (2019) 903–912, https://doi.org/10.1016/j.solener.2019.11.037.
[23] W. Oh, S. Kim, S. Bae, N. Park, Y. Kang, H.S. Lee, D. Kim, The degradation of multi-crystalline silicon solar cells after damp heat tests, Microelectron. Reliab. 54 (2014) 2176–2179, https://doi.org/10.1016/j.microrel.2014.07.071.
[24] X. Li, Y. Yang, K. Jiang, S. Huang, W. Zhao, Z. Li, G. Wang, A. Han, J. Yu, D. Li, F. Meng, L. Zhang, Z. Liu, W. Liu, Potential-free sodium-induced degradation of silicon heterojunction solar cells, Prog. Photovoltaics Res. Appl. (2023), https://doi.org/10.1002/pip.3698.
[25] Oxford Instruments, Energy Dispersive X-ray Spectroscopy (EDS), (n.d.). https://nano.oxinst.com/products/eds/(accessed February 3, 2025).
[26] M.A. Green, Solar Cells: Operating Principles, Technology, and System Applications, Prentice-Hall, Inc., Englewood Cliffs, NJ, 1982.
[27] F.A. Stevie, Secondary Ion Mass Spectrometry: Applications for Depth Profiling and Surface Characterization, Momentum Press, 2015.
[28] J.C. Vickerman, B. David (Eds.), ToF-SIMS Materials Analysis by Mass Spectrometry, second ed., IM Publications and Surface Spectra, 2013.
[29] R.G. Wilson, F.A. Stevie, C.W. Magee, Secondary Ion Mass Spectrometry: A Practical Handbook for Depth Profiling and Bulk Impurity Analysis, Wiley, 1989.
[30] J.I., N.D.E., M.J.R., R.N.W., S.J.H.J., J.D.C. Goldstein, Scanning Electron Microscopy and X-Ray Microanalysis, springer, 2017.
[31] J.A. Small, The analysis of particles at low accelerating voltages (10 kV) with Energy dispersive X-ray spectroscopy (EDS), J Res Natl Inst Stand Technol 6 (2002) 555–566.
[32] H. Daido, M. Nishiuchi, A.S. Pirozhkov, K. Kanayat, S. Okayama, Penetration and Energy-Loss Theory of Electrons in Solid Targets You May Also like Review of Laser-Driven Ion Sources and Their Applications Penetration and Energy-Loss Theory of Electrons in Solid Targets, 1972.
[33] J.I. Goldstein, D.E. Newbury, J.R. Michael, N.W.M. Ritchie, J. Henry, J. Scott, D.C. Joy, Scanning Electron Microscopy and X-Ray Microanalysis, n.d.[.
[34] ASTM International, Guide for Quantitative Analysis by Energy-Dispersive Spectroscopy, ASTM International, West Conshohocken, PA, 2012, https://doi.org/10.1520/E1508-12.
[35] S.J.B. Reed, Electron Microprobe Analysis and Scanning Electron Microscopy in Geology, second ed., Cambridge University Press, Cambridge, 2005.
[36] P.J. Potts, A Handbook of Silicate Rock Analysis, Springer Science & Business Media, 1992.
[37] X. Li, W. Liu, W. Zhao, S. Huang, W. Huang, J. Shi, A. Han, J. Li, H. Chen, L. Zhang, F. Meng, Z. Liu, Highly crystallized tungsten doped indium oxide film stabilizes silicon heterojunction solar cells in sodium environment, Sol. Energy Mater. Sol. Cell. 233 (2021), https://doi.org/10.1016/j.solmat.2021.111387.
[38] X. Wu, X. Wang, R. Lv, H. Song, Y. Yu, C. Sen, Y. Cheng, M.U. Khan, A. Ciesla, T. Xu, G. Zhang, B. Hoex, Unveiling the degradation mechanisms in silicon heterojunction solar cells under accelerated damp-heat testing, Sol. Energy Mater. Sol. Cell. 282 (2025), https://doi.org/10.1016/j.solmat.2024.113325.
[39] K. Jiang, Y. Yang, Z. Yan, S. Huang, X. Li, Z. Li, Y. Zhou, L. Zhang, F. Meng, Z. Liu, W. Liu, Balance of efficiency and stability of silicon heterojunction solar cells, Sol. Energy Mater. Sol. Cell. 243 (2022), https://doi.org/10.1016/j.solmat.2022.111801.
[40] C. Sen, X. Wu, H. Wang, M.U. Khan, L. Mao, F. Jiang, T. Xu, G. Zhang, C. Chan, B. Hoex, Accelerated damp-heat testing at the cell-level of bifacial silicon HJT, PERC and TOPCon solar cells using sodium chloride, Sol. Energy Mater. Sol. Cell. 262 (2023) 112554, https://doi.org/10.1016/j.solmat.2023.112554.
[41] X. Wu, C. Sen, X. Wang, Y. Cheng, Y. Wu, H. Song, R. Lv, T. Huang, Y. Yu, T. Xu, B. Liao, S. Ma, M.U. Khan, A. Ciesla, G. Zhang, B. Hoex, Unveiling the Origin of Metal Contact Failures in TOPCon Solar Cells through Accelerated Damp-Heat Testing, (n.d.). https://doi.org/10.4229/EUPVSEC2023/3AV.2.41.

[42] C. Sen, C. Chan, X. Wu, H. Wang, M.U. Khan, L. Mao, J.-N. Jaubert, F. Jiang, G. Zhang, B. Hoex, The role of Na + contamination in humidity-induced degradation in silicon HJT cells, in: Asia-Pacific Solar Research Conference, 2022.
[43] M.U. Khan, C. Sen, C. Chan, M. Abbott, G. Poduval, Y. Wu, R. Lv, G. Zhang, B. Hoex, Supercharging cell-level potential-induced degradation (PID) testing using a salt-enriched hybrid polymer layer, Sol. Energy Mater. Sol. Cell. 260 (2023) 112479, https://doi.org/10.1016/j.solmat.2023.112479.
[44] S. Yamaguchi, C. Yamamoto, K. Ohdaira, A. Masuda, Reduction in the short-circuit current density of silicon heterojunction photovoltaic modules subjected to potential-induced degradation tests, Sol. Energy Mater. Sol. Cell. 161 (2017) 439–443, https://doi.org/10.1016/j.solmat.2016.12.027.